



Cyclical hydraulic pressure pulses reduce breakdown pressure and initiate staged fracture growth in PMMA

Julien Mouli-Castillo · Jackie E. Kendrick · Alexander Lightbody ·
Andrew Fraser-Harris · Katriona Edlmann ·
Christopher Ian McDermott · Zoe Kai Shipton

Received: 28 September 2022 / Accepted: 10 January 2024
© The Author(s) 2024

Abstract Using unique experimental equipment on large bench-scale samples of Polymethylmethacrylate, used in the literature as an analogue for shale, we investigate the potential benefits of applying cyclical hydraulic pressure pulses to enhance the near-well connectivity through hydraulic fracturing treatment. Under unconfined and confined stresses, equivalent to a depth of up to 530 m, we use dynamic high-resolution strain measurements from fibre optic cables, complemented by optical recordings of fracture development, and investigate the impact

of cyclical hydraulic pressure pulses on the number of cycles to failure in Polymethylmethacrylate at different temperatures. Our results indicate that a significant reduction in breakdown pressure can be achieved. This suggests that cyclic pressure pulses could require lower power consumption, as well as reduced fluid injection volumes and injection rates during stimulation, which could minimise the occurrence of the largest induced seismic events. Our results show that fractures develop in stages under repeated pressure cycles. This suggests that Cyclic Fluid Pressurization Systems could be effective in managing damage build-up and increasing permeability. This is achieved by forming numerous small fractures and reducing the size and occurrence of large fracturing events that produce large seismic events. Our results offer new insight into cyclical hydraulic fracturing treatments and provide a unique data set for benchmarking numerical models of fracture initiation and propagation.

Supplementary Information The online version contains supplementary material available at <https://doi.org/10.1007/s40948-024-00739-z>.

J. Mouli-Castillo (✉) · J. E. Kendrick · A. Lightbody ·
A. Fraser-Harris · K. Edlmann · C. I. McDermott (✉)
School of Earth Sciences, The University of Edinburgh,
Edinburgh, Scotland, UK
e-mail: Julien.mouli-castillo@glasgow.ac.uk

C. I. McDermott
e-mail: christopher.mcdermott@ed.ac.uk

J. Mouli-Castillo
James Watt School of Engineering, The University
of Glasgow, Glasgow, Scotland, UK

J. E. Kendrick
Department of Earth and Environmental Science, Ludwig-
Maximilians-Universität München, Munich, Germany

Z. K. Shipton
Department of Civil and Environmental Engineering,
University of Strathclyde, Glasgow, Scotland, UK

Article Highlights

- Cyclical Hydraulic Pressure Pulses (CHPP) can reduce the breakdown pressure required to fracture PMMA.
- CHPP have potential to reduce peak power consumption to achieve failure and increase permeability of a rock, with positive implications for geothermal applications.

- CHPP induced multi-staged fracture propagation, implying an enhanced ability to control damage initiation by hydraulic fracturing.

Keywords Geo-energy · Pulsed pumping · Breakdown pressure · Geothermal

1 Introduction

Our investigation is rooted in the need to find more efficient ways of accessing or percolating subsurface fluids. Many geo-energy technologies are contingent on being able to inject and extract fluids from the subsurface at minimal costs. This is even more important at a time when the cost of energy is increasing, which puts technologies required to decarbonise our societies at risk of becoming uncompetitive. Fluids can be injected or extracted from the subsurface using wells. These wells are expensive to drill and therefore finding ways to increase their productivity is critical to enabling long term geo-energy operations. The critical parameters affecting the rate at which fluids can be injected or extracted from the rock mass at the base of the borehole are the differential pressure between the fluid in the well and the fluid in the rock mass, and the permeability of the rock mass. Usually, permeability will reduce through time as fines and drilling waste clog up flow pathways in the vicinity of the well. Hence, a greater pressure differential is required to move the fluid in and out of the rock, this results in increased requirements in terms of the pumping equipment at the surface—which comes at a cost. Hence, finding ways to increase the permeability of the rock mass surrounding the well is critical.

A number of recent studies have proposed that Cyclical Hydraulic Pressure Pulse (CHPP) treatment can be used to enhance the permeability of the subsurface (Hofmann et al. 2018a; b; Zang et al. 2019; Zimmermann et al. 2019). The permeability of the near well field (within ~1 m), is dominant in controlling the fluid connectivity of the well to the wider rock mass. Through improved control of the hydraulic fracturing process and creation of new fractures in the near well field, experimental results indicate that the connectivity to the surrounding rock mass can be increased, and the occurrence of microseismic events can be significantly reduced (Hofmann et al. 2018a,

b; Zhuang et al. 2018). In detail, in such scenarios the seismic b-value may be reduced even if the stress released by fracturing remains the same; resulting from a reduction in the proportion of large events and more frequent small events, which can produce more complex fracture networks (Zang et al. 2021). This technology is highly relevant to the development of geo-energy industries such as the use of aquifers and near surface geothermal energy extraction, storage of recycled heat, compressed air storage, hydrogen storage and geological carbon dioxide storage, all vital aspects of a diverse geo-energy portfolio to reduce societies' energy carbon footprint. Furthermore, it can also improve access to water resources, particularly in granitic regions (Cobbing and O Dochartaigh 2007).

Attention must be given to means of controlling fracture propagation behaviour, since it is important to ensure both that the target rock has an increased permeability and that the fracture does not propagate too far, so as to lead to a safety risk. Hydraulic fracture propagation work using a laboratory simulation approach has been carried out (Wu et al. 2007; Guruprasad et al. 2012; Frash 2014; Guo et al. 2018; Mohammad et al. 2018; Wanniarachchi et al. 2018; Xing 2018; Liu et al. 2019). Simulation investigations were performed on limestone, granite, concrete and PMMA, showing that re-stimulation of existing fractures increased injectivity (Frash 2014). Wanniarachchi (2018) studied the influence of fracturing fluid on the fracture pattern and permeability of fractured rock, finding that when using foam, induced fractures had greater surface area and complexity. By means of the phase field numerical method, Liu et al. (2019) investigated how natural cavities affect the propagation of hydraulic fractures, finding that when reducing the Young's modulus ratio between the cavity and rock mass the deviation of the fracture became significant.

Building on this work, we investigate how the peak pressure and minimum pressure induced by CHPP within a borehole affect the number of cycles to failure and the development of the fracture in large scale thermoplastic polymer Polymethylmethacrylate (PMMA) samples (Ø 200 mm, and length 200 mm) using a novel experimental setup. Fluid pressure, optical footage, and high-resolution strain measurements are combined to present a multi-faceted interpretation of multi-stage hydraulic fracture growth resulting from pressure pulses. The PMMA used here is often

cited as a shale analogue material, and is regularly used in experiments to investigate natural fracture processes in rocks (Lee and Jeon 2011; Gomez Rodriguez et al. 2016; Khadraoui et al. 2020). It is considered an analogue to shale in terms of its mechanical properties, low matrix permeability, elasticity, and fracture toughness (Senseny and Pfeifle 1984; Khadraoui et al. 2020). While PMMA does not contain the same internal variability as shale, its homogeneity and lack of pre-existing fracture networks provides a useful benchmark for investigating the effects of those fracture networks in real rocks (Roshankhah et al. 2018), and here provides us with the structural homogeneity to explore the impact of cyclic hydraulic pressure pulses within a repeatable material. Shale is highly heterogeneous and mechanically anisotropic (Ibanez and Kronenberg 1993), it is also friable and deteriorates rapidly under laboratory conditions, and as such it is very challenging to recover and prepare intact shale samples at our sample size.

PMMA has been extensively studied in the literature due to its viability as a rock analogue and its medical and military applications. PMMA studies that report a stress–strain curve indicate consistent observations, with the elastic limit of the material extending up to around 80 MPa in uniaxial compression (Swallowe and Lee 2006). Fatigue properties of PMMA have been determined using a standardised dog-bone tensile test where the sample is pulled in one direction until failure occurs (Carnelli et al. 2011). Other investigations assessed the creep of PMMA under cyclic loading at different temperatures, concluding that both temperature and loading path impact the strain evolution (Liu et al. 2008). However, the minimum stress applied in those cyclic assessments was close to 0 MPa which is not representative of borehole conditions used for geo-energy applications. Gurusprasad et al. (2012) determined that injection hole diameter, pressure and temperature can all lead to an increase in induced fracture length. Xing et al. (2018) emphasised the role of net pressure and stress on fracture growth, using a transparent polyurethane material that enables the fracture geometry to be clearly observed in all directions.

This optical transparency property of PMMA offers the opportunity to image the growth of fractures, and Khadraoui et al. (2020) demonstrated the use of PMMA for visual inspection of hydraulic fracture propagation inside 50 mm diameter samples

during experimental investigation. Previous work used PMMA as a benchmark material against which to compare shales through the investigation of monotonic hydraulic fracturing. It imaged a complex interaction between the injected fluid, the pre-existing natural fractures, and the hydraulically induced fractures (Roshankhah et al. 2018). This work by Roshankhah (2018) highlighting the interaction with pre-existing natural fractures is echoed by the work by Mighani (2018) investigating the interaction between hydraulic fractures and pre-existing fractures undertaken using PMMA. Multiple examples of material fatigue characterisation using PMMA plates and dog-bone shaped samples have also been conducted (Huang et al. 2014). Gan et al. (2015) investigated the breakdown pressures during hydraulic fracturing using PMMA, drawing particular attention to the influence of the fluid's interfacial tension (IFT) on breakdown pressure; the IFT of a fluid controls the permeation of the fluid into the matrix and they observed that breakdown pressure of impervious cases is approximately twice as large as that of the permeable case. This highlights the importance of the materials' permeability when attempting to initiate a fracture.

PMMA is therefore a well characterised potential shale analogue in which to investigate CHPP effects on breakdown pressure and fracture. Our work provides experimental data characterising the sample behaviour under CHPP for validation of numerical models used to investigate the benefits of soft cyclic treatment on hydraulic fractures. This work builds upon the significant characterisation of PMMA in response to various stress–strain conditions presented above, and adds to the literature on the application of CHPP by investigating PMMA under conditions analogous to those that are encountered by a borehole at depth. Furthermore, this material being very repeatable improves the reliability of defined trends. The experiments use 200×200 mm cylindrical PMMA samples and apply an axial stress of 8 MPa (equivalent to the effective axial load of a 530 m deep borehole), with fluid pressure cycled inside a central 6 mm diameter, 120 mm long borehole. The borehole internal surface is not totally regular due to being drilled, and to some extent can be considered representative of the rough uneven surface that would be present in an uncased borehole or a crack.

We developed a pressure-controlled delivery system to investigate the effect of square waves on the

fatigue life of PMMA. This furthers the literature, which mostly focusses on monotonic, or sinusoidal, variation in pressure due to the predominance of flow rate control. We can therefore induce a square wave pressure cycle with the pump operating at a constant flow rate. This is important when considering that pressure pulse targeting induced by valve shifting of a high and low pressure line to allow the pump to perform at a constant flow rate would result in the borehole zone targeted for fracturing experiencing high pressure changes over short time periods, akin to a square wave pattern. We control both mean pressure and cycle amplitude. This affords a new insight by studying a new type of cycle. Uniquely, our experimental observations include fibre optic strain measurement around the circumference of the sample, providing high density strain measurements (every 2.6 mm) around the sample's exterior, at 25 Hz frequency, allowing the temporal constraint of fracture development to be made for the first time. We define the initiation of a fracture as the onset of a significant fluid pressure drop in the borehole. The test concludes once the sample has been fractured all the way to the margin.

2 Materials and methods

2.1 Sample characterisation

The samples are made from a cast PMMA bar purchased from Clear Plastic Supplies¹. Our use of cast PMMA bars, which lack inherent pore structures, was a deliberate choice to isolate and study particular variables of the hydraulic fracturing process under controlled conditions with a homogeneous and repeatable material. While we recognise that pore structure and rock mass composition are critical to the fracking process, our research aims to first understand the fundamental mechanics of fracture propagation and fluid flow in a simplified system. The transparency of PMMA allows for real-time, in-situ visualisation of these phenomena, which is often obscured in natural shale samples. The bar was cut to 200 mm lengths and in each sample a 6 mm diameter borehole was drilled from the centre of its top face down to 80 mm

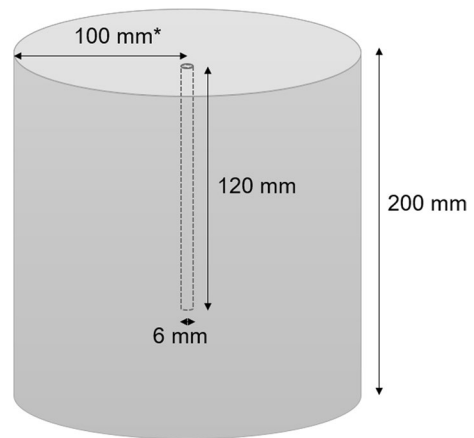


Fig. 1 Sample dimensions. In the confined test the sample diameter was reduced to 193.75 mm to accommodate a rubber jacket within the GREAT cell

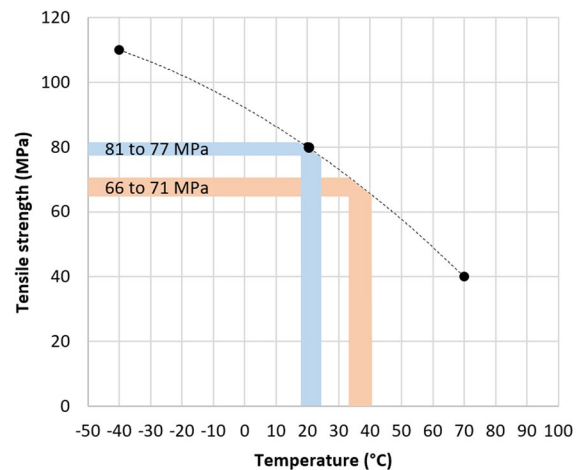


Fig. 2 Tensile strength of PMMA as a function of temperature from manufacturer's data in black. Dashed line represents polynomial interpolation from manufacturer's data. Blue shaded band indicates the ambient temperature experimental conditions, and the orange shaded area the heated experimental conditions chosen for our study

from the base (Fig. 1). This borehole depth (120 mm) was selected to allow for a larger volume for fracture propagation because the fracture usually propagates upwards from the base of the borehole (Zhuang et al. 2020). The following material properties are provided by the manufacturer: a Poisson's ratio of 0.37 comparable to shale (Molina et al. 2017), a temperature-dependent tensile strength (see Fig. 2), which we

¹ (<http://www.clearplasticsupplies.co.uk>)

used to define the tensile strength at our experimental temperatures of 21 and 40 °C, giving 77–81 MPa and 66–71 MPa, respectively (Fig. 2). We use these two temperature conditions to simulate the effect of pulsed pumping for different host rock conditions, in which the strength and elastic parameters differ, to explore the viability of the approach under different scenarios.

We further tested the elastic mechanical properties by defining the Young's modulus of the PMMA. The PMMA was taken from the same rod used to create the large samples. Using an 'Instron model 5969' 50 KN uniaxial press in the Volcanology and Geothermal Research Laboratory at the University of Liverpool, we non-destructively loaded and unloaded a core of PMMA of 40 mm in diameter by 105 mm in length under the following strain rates: 10^{-2} , 10^{-3} , 10^{-4} , 10^{-5} s⁻¹ to 25 MPa. Position and load (cf. stress given the constant contact area) were monitored at a frequency of 100 Hz, and the compliance of the machine was corrected for in real-time by the Bluehill® software (Instron) using a series of calibrations run with no sample at the same displacement rates and target load.

2.2 Hydraulic fracture testing equipment

To investigate the impact of CHPP on materials from a central borehole, we designed, further developed, and utilised three key experimental devices:

- (1) Cyclic fluid pressurisation system
- (2) An unconfined uniaxial rig
- (3) The Geo Reservoir Experimental Analogue Technology (GREAT) Cell (McDermott et al. 2018; Fraser Harris et al. 2020)

2.2.1 Cyclic fluid pressurisation system

A pump was developed to create the cyclical pressure pulses that were applied to the sample. A LabVIEW program was developed to control the pump and switched from high to low pressure every 3.57 s, a cycle frequency of 0.14 Hz. This frequency ensured that the sample did not heat up via internal friction (i.e. hysteretic heating). This heating is insignificant at frequencies below 0.5 Hz (Editorial Committee of Fatigue and Fracture Atlas of PMMA 1987). Water

was used as the working fluid, with an estimated viscosity of around 1.0 mPa.s at ambient temperature (about 21 °C) and 0.7 mPa.s at 40 °C. The temperature was recorded at 1 Hz sampling frequency. The LabVIEW controller allowed the fluid pressure to be monitored at 500 Hz, which is several orders of magnitude greater than the cycle frequency. This enabled the pressure drop after failure initiation to be recorded.

2.2.2 Unconfined uniaxial rig

Experimental equipment was designed to recreate the axial stress experienced by a near borehole environment using CHPP. The equipment consisted of a 200 mm wide cylindrical stainless-steel platen to apply load to a sample. The load, which we converted to an axial stress, was manually controlled with a hand pump delivering oil pressure to a piston in contact with the top of the platen. A LabVIEW controller calculates the axial stress delivered with a visual graphical feedback for the user to control it during the experiment. The axial stress, held constant throughout the experiments, was recorded at a rate of 1 Hz to monitor its consistency.

The platen allowed for fluid injection through a borehole located at the centre of the sample, with a BS113 nitrile o-ring providing a face seal between the platen and the sample around the borehole. Optical fibre strain gauges, bonded to the sample using Loctite® Super Glue to ensure optimal coupling, measured the circumferential strain during the experiment. Fibre-optic measurements were made using a fibre optic strain gauge coupled with a LUNA module and the ODISI-B acquisition software sampling at 25 Hz, the maximum allowable by the hardware (Gifford et al. 2007). The rig was radially unconfined to allow the use of Go-Pro optical cameras with 240 frames per seconds to capture the development of the fracture.

2.2.3 GREAT cell

The Geo-Reservoir Experimental Analogue Technology (GREAT) cell (McDermott et al. 2018; Fraser-Harris et al. 2020) was used to conduct the triaxial test. It is designed to recreate subsurface conditions in the laboratory up to a depth of ~3000 m on ~200 mm diameter cylindrical samples. The equipment has the

ability to induce polyaxial stresses experienced in the subsurface ($\sigma_1 \neq \sigma_2 \neq \sigma_3$). To retain a differential between the radial and axial stresses of 8 MPa as in the unconfined tests, the confined test was conducted with a uniform radial stress ($\sigma_2 = \sigma_3$) of 4 MPa and an axial stress of 12 MPa. This allowed us to evaluate its effect and develop the experimental protocol and control systems to combine the Cyclic Fluid Pressurisation System described above with the GREAT Cell. In the GREAT cell, radial pressure was applied via 8 opposing pairs of hydraulic bladders supplied by 8 pumps. The pressure in the bladders was automatically controlled by a PLC control system at a frequency of 1 Hz with an accuracy of 0.05 MPa. Axial stress was applied through a linear actuator under stroke control. Using the same configuration as in the unconfined set-up, strain was measured with an acquisition rate of 25 Hz.

2.3 Hydraulic fracture procedure

Before the sample was placed into the sample assembly, the central borehole was primed with a syringe and any bubbles in the water were removed by gently stirring. The top platen was lowered onto the sample until a load of about 0.1 MPa was applied. The swage lock fitting connecting the fluid line to the platen was then loosened slightly to monitor extraction of any remaining trapped air. Then the fluid line to the sample was opened and the pump and valves set to flow water into the sample. The control system was used to ensure that the pressure remained close to atmospheric. When the bubbles from the loosened fitting had stopped and a steady stream of water drops developed, indicating all air had been purged from the system, the pump was stopped, the fitting tightened, and then the isolation valve to the sample shut before proceeding.

2.3.1 Unheated unconfined monotonic tests

An initial radially unconfined monotonic hydraulic fracturing test was conducted under an axial stress of 8 MPa to determine the breakdown pressure with a non-pulsed fluid. This value was needed to define the conditions used in all subsequent cyclic tests. The sample was loaded into the unconfined rig, the borehole was primed with water and ambient temperature and the monitoring and logging equipment

was started. The sample was loaded to 8 MPa using an axial piston operated by an oil hand pump. The water was injected at a rate of 1 ml/min under ambient temperature conditions of 21 °C. Fluid pressure in the borehole rose until failure occurred at a fluid pressure of 37.85 MPa. The internal fluid pressure in the borehole results in a radial stress of - 37.8 MPa and a hoop stress of 37.7 MPa. This results in a maximum differential stress of approximately 76 MPa. This differential stress matches the tensile strength of the PMMA material in this study, hence indicating a good match between the experimental data and the manufacturer's.

2.3.2 Unheated unconfined cyclic tests

First the logging equipment was set to record. The sample was loaded axially in the unconfined rig described in Sect. 2.2.2, until a constant axial stress of 8 MPa was achieved. This load was maintained throughout the cycling of the fluid pressure using the manual oil pump. The fluid injection pump was turned on and the back pressure regulators adjusted to the desired maximum and minimum pressures. Maximum and minimum pressures were chosen as a fraction of the monotonic breakdown pressure according to our experimental programme shown in Table 1. The experiment started when the valve between the fluid pressure transducer and the platen was opened, exposing the sample to the cyclic fluid pressure. At this stage the back pressure regulators could require minor adjustments to account for any small changes to the maximum and minimum pressures caused by the friction in the portion of the fluid line between the valve and the sample. The sample was exposed to cycles consisting of 3.57 s of high fluid pressure, followed by 3.57 s of low fluid pressure.

2.3.3 Heated unconfined cyclic tests

First the platens and samples were heated to 40 °C in an oven and once they had reached the target temperature the logging equipment was set to monitor. The bottom platen was taken from the oven and placed onto the rig. The sample was then placed onto the bottom platen. The borehole was primed as described previously. A heating band with thermocouple PID temperature control was attached around the sample using thermal-resistant tape. The sample, with fibre

Table 1 Experimental matrix

ID	Maximum pressure	Minimum pressure	Mean pressure	Cycle pressure amplitude	Confining pressure	Temperature	Rig	Type
NA	MPa	MPa	MPa	MPa	MPa	°C	NA	NA
0 ^a	38	N/A	N/A	N/A	N/A	Ambient	Unconfined	Monotonic
1	29	15	22	14	N/A	Ambient	Unconfined	Cyclic
2	28	16	22	12	N/A	Ambient	Unconfined	Cyclic
3	27	17	22	10	N/A	Ambient	Unconfined	Cyclic
4	26	18	22	8	N/A	Ambient	Unconfined	Cyclic
5	26	18	22	8	N/A	Ambient	Unconfined	Cyclic
6	24	14	19	10	N/A	Ambient	Unconfined	Cyclic
7	30	20	25	10	N/A	Ambient	Unconfined	Cyclic
8	26	18	22	8	N/A	40 °C	Unconfined	Cyclic
9	27	17	22	10	N/A	40 °C	Unconfined	Cyclic
10	29	15	22	14	N/A	40 °C	Unconfined	Cyclic
11	31	21	26	10	4	Ambient	GREAT Cell	Cyclic

^aIndicates the monotonic test which was conducted prior to the main suite of experiments to characterise the tensile strength of the material

optic cable, was loaded as described previously, and the remaining heating bands were attached to the top and bottom platens. The thermocouples from the National Instrument module (NI 9213) were taped to the top and bottom platen, and at three equidistant points along the height of the sample, and an insulating jacket was placed around the sample and platens to ensure the temperature remained stable and at the required 40 °C set point. It was important to ensure the fluid temperature was the same as the sample temperature and this was achieved by using a heated plate with a magnetic stirrer to heat the water. The water was circulated in the pipe work, which was heated with temperature-controlled heating bands until it reached a steady temperature within error of the target temperature (± 3 °C). The same test procedure as in the unheated test was then applied.

2.3.4 Confined cyclic test

The GREAT cell was loaded with a PMMA sample 193.75 mm in diameter by 200 mm height, with an optic fibre attached around the circumference of the sample (McDermott et al. 2018). Sixteen hydraulic cushions then exerted a controlled radial force on the GREAT cell to create the radial isotropic stress field required. The cyclic pressurisation system equipment was connected to the top platen inlet which had the same design as described in the unconfined system.

The experiment was started by applying an axial stress of 8 MPa, exposing the sample to the same conditions as in the unconfined experiments. The sample was given 10 min to stabilise, indicated by both stable axial stress and absence of strain change or creep on the fibre optic strain gauge. The radial stress was then applied at 4 MPa. Again, after monitored stabilisation the axial stress was increased to 12 MPa, to retain a differential stress of 8 MPa, comparable to the unconfined experiments. Due to the importance in the differential between the fluid pressure and the confinement, the borehole pressures in this experiment were also increased by 4 MPa, to retain the same differential pressure as in the unconfined test 3, also conducted at ambient temperature. The Cyclic Fluid Pressurisation System developed was used, applying the same procedure as described in Sect. 2.3.2 to deliver pressure pulses to the sample.

2.4 Modelling methodology

To determine the likely stress state at the borehole wall during the high and low pressure parts of the cycles in each experiment, the OpenGeoSys coupled process simulator was used (Kolditz et al. 2012). We used the benchmark validated elastic solution since, according to the Lamé Solution theory for thick-walled cylinders, the differential stress state at the borehole wall was lower than the tensile strength of

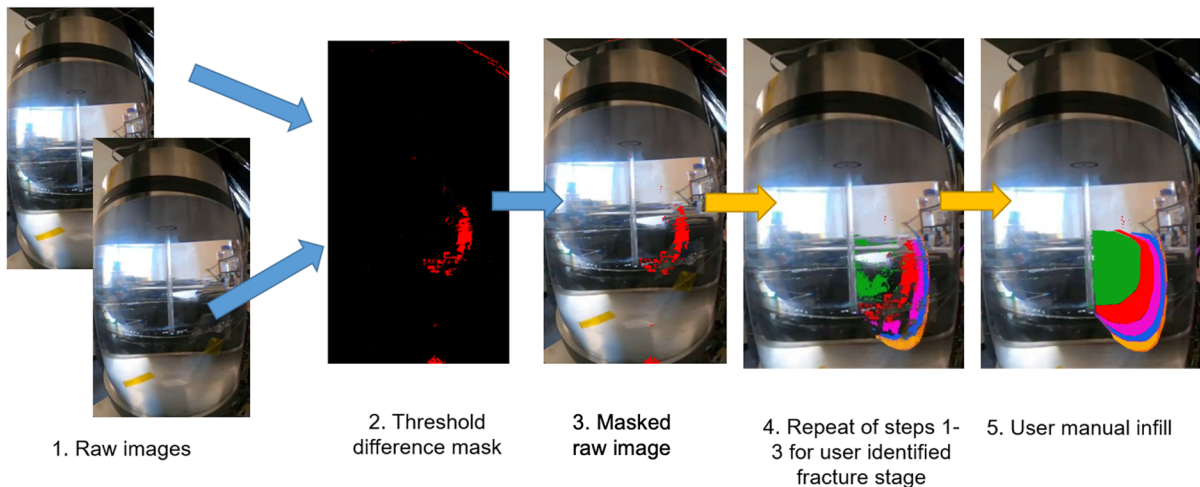


Fig. 3 Image processing methodology. Imaged sample was 200 mm in diameter and 200 mm in height. Colours represent the various segmentation steps performed between successive images taken at 240 fps. Step 1 presents two examples of raw images extracted from the GoPro video. Step 2 represents the threshold difference mask applied to the image to highlight pixels of different colour in red and similar pixels in black.

the material. Here the differential stress is defined as the difference between the radial and tangential stresses at any given point on the borehole wall. The Poisson's ratio obtained from the manufacturer was 0.37. A 2D-axisymmetric model was used to reduce computing time. The spatial discretisation of the model was achieved by generating a mesh of triangles using GMSH (Geuzaine and Remacle 2009), with an element side length of 0.5 mm at the borehole and 8 mm at the sample edge (see Additional file 1: Fig. 1). This was suitable due to the high homogeneity of the PMMA. The borehole tip was approximated to a quadrant of 3 mm radius.

2.5 Optical monitoring and image segmentation

We monitored the experiments using a GoPro Hero 8 Black 2 at 240 fps. Where a fracture propagated at a favourable angle to the camera position, the fracture growth could be monitored. The video frames were extracted using OpenCV (Bradski 2000) Python Library (Fig. 3, step 1). The real colour images were then processed by computing the difference between an image and the one from the previous frame (Fig. 3, step 2). The 'difference image' was converted to greyscale and a threshold was applied to it using the

Step 3 shows how the coloured different pixel mask is applied to the original image. Step 4 replicates the previous steps (with different colours for legibility) to show the propagation of the fracture. Step 5 indicates how the user manually infills gaps in the fracture propagation extracted automatically by using the background image as a reference

inbuilt `THRESH_BINARY_INV` and `THRESH_OTSU` functions. The threshold mask was coloured red to help distinguish the fracture growth. The mask was then applied back onto the image in real colour (Fig. 3, step 3). Further to these automatic steps, the frames in which fracture growth was identified by the user were selected and the operation described above was repeated with different coloured filters (Fig. 3, step 4). The output was opened in a photo processing tool and the areas of growth manually infilled, based on the thresholding information extracted automatically (Fig. 3, step 5). The pixels from each coloured area were then counted by using the colour select toolset to have a zero tolerance.

3 Results

3.1 Young's modulus

We defined the Young's modulus from the linear elastic portion of the stress-strain curves during compressive loading of cylinders of PMMA to 25 MPa at strain rates of 10^{-5} – 10^{-2} s^{-1} . We found that the Young's Modulus shows an apparent increase with increasing strain rate (Fig. 4).

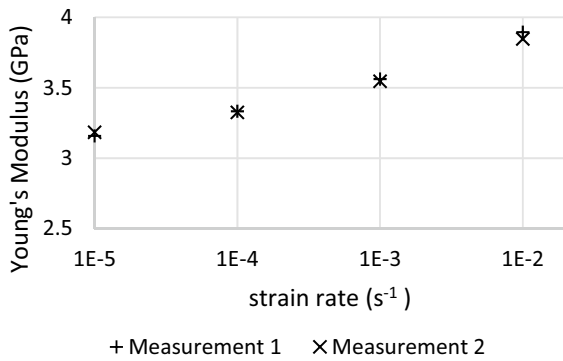


Fig. 4 PMMA Young's Modulus against deformation rate highlighting the rate dependence of the material

3.2 Borehole simulations

In order to understand better the stress state in the borehole during the hydraulic fracture tests, we performed numerical simulations using OpenGeoSys. The borehole simulation results for the confined, unconfined, heated, and un-heated experiments yielding the same differential borehole stress state, along with the reference monotonic test, are presented in Fig. 5. We define the differential stress as the difference between the radial and tangential stresses at any given point on the borehole wall. Experiment 0^a is a

monotonic test, hence the minimum differential stress at the start of the experiment is not of interest for the purpose of determining fracture stress conditions: it fractured when the fluid pressure reached 38 MPa. In Test 3, we carried out an unheated and unconfined procedure, resulting in a differential borehole stress state equivalent to what was seen in Test 11. The fluid pressure ranged between 17 and 27 MPa, resulting in an amplitude of 10 MPa. This test did not involve any confining stress (i.e. atmospheric pressure) and was performed at normal room temperature using the unconfined rig. For Test 9, we applied the same conditions as Test 3, except for the temperature which was raised to 40 °C in the unconfined setup. Test 11, on the other hand, was a confined experiment. Here, the fluid pressure varied from 21 to 31 MPa, also with a 10 MPa amplitude, but the sample experienced a confining stress of 4 MPa. This was carried out at normal room temperature in the GREAT Cell. Additional details on these and other experiments can be found in the Additional file 1: Fig. 2.

The differential stress at the wellbore wall (Fig. 5) is approximately twice as large as the wellbore pressure. The results show that the highest differential stress state is achieved during the high-pressure parts of the cycles as expected from the Lamé Equations. The shear stresses we see developing at the base of

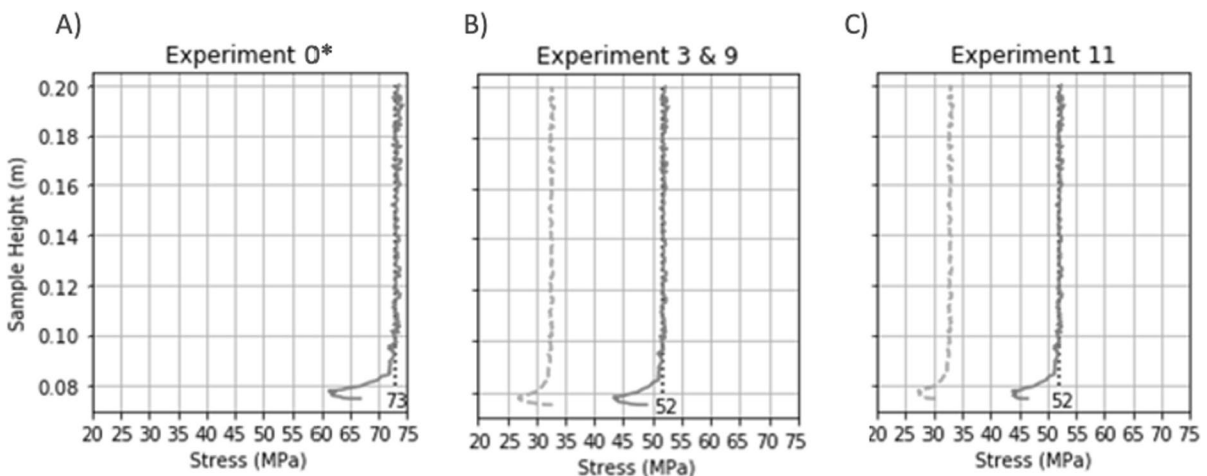


Fig. 5 Simulations using OpenGeoSys. **A** Experiment 0^a is a monotonic test. **B** Experiment 3 is the unconfined and unheated test. Experiment 9 is the heated experiment with the same cycles as Experiment 3. **C** Experiment 11 is the confined test in the GREAT Cell. The solid lines indicate the differen-

tial stress ($\sigma_1 - \sigma_3$) at the borehole wall during the high-pressure part of the cycle. The dashed lines indicate the differential stress at the borehole wall during the low-pressure part of the cycle. The median value of the maximum pressure rounded to the closest MPa is indicated as labelled vertical dotted line

the borehole are because of the coordinate rotation, where the normal stress of the borehole is no longer being applied in a radial direction, but rather being applied normal to the wall of the borehole, which at the base was assumed to be a half-sphere in the modelling to account for the shape of the drill bit and to avoid numerical stress concentration which would result from a flat base. This change in the direction in which the stress is applied leads to a rotation of the stress field, which in the x_y coordinate system leads to shear stress being developed. The modelled values are close to 3.5% lower than Lamé's analytical solution in the axial portion of the borehole wall. In the Lamé solutions for thick-walled cylinders, the stress distribution is independent of material's rheology and is purely a function of the cylinder's geometry and the pressure boundaries. We have also conducted a few simulations with a much lower Poisson's Ratio. As expected, this only affected the response in the base of the borehole and reduced the maximum differential stress.

3.3 Hydraulic cyclic pressure pulsing

3.3.1 Timing of fracture development

Throughout all tests the first indication of sample failure was indicated by a drop in fluid pressure below the low pressure line's set point. We can observe from Fig. 6, which displays the fluid pressure data from the penultimate cycle prior to failure initiation, that all experiments fail during the 'high-pressure' part of the cycle. This is true for the 0.14 Hz frequency we tested. Lower frequencies might allow more time for the sample to fail during the low pressure portion of the cycle.

Table 2 presents the number of cycles to failure for each experiment. The results indicate that increasing the amplitude of the cycle reduces the number of cycles to failure. However, increasing the mean pressure (and therefore maximum pressure, given the same amplitude) has a much greater impact on the reduction of number of cycles to failure. This is consistent with the fact that increasing the mean pressure raises both the minimum and maximum differential stress at the wellbore wall, whilst increasing the amplitude increases the maximum differential stress, but reduces the minimum one. Hence, we see a strong correlation between pressure amplitude and cycles to

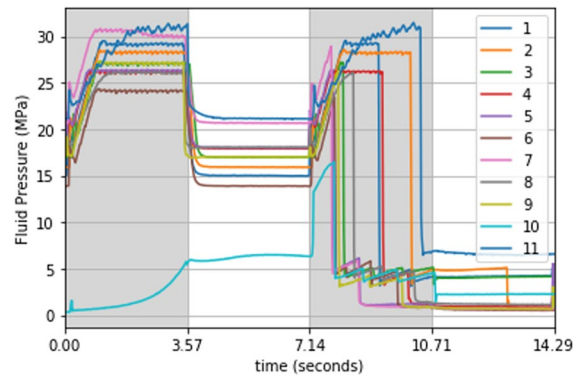


Fig. 6 Plot of the fluid line pressure from the penultimate cycle before failure and final cycle, showing the fracture time of each experiment (rapid pressure drop). Experiment 10 failed during the first cycle, before it could reach its set cycling pressure. This explains the lower failure value for that experiment. Therefore, for Experiment 10 we see the first, rather than penultimate cycle. In addition, we can see the gradual pressurisation happening during the high-pressure portions of the cycle, up until its failure before it reaches the set point pressure. The figure shows that failure occurs during the high-pressure part of the cycle in all experiments. The time axis is relative to the start of the penultimate cycle before failure initiation

failure, as well as between maximum pressure and cycles to failure, which we explore further in the following sections.

3.3.2 $S-N$ curves

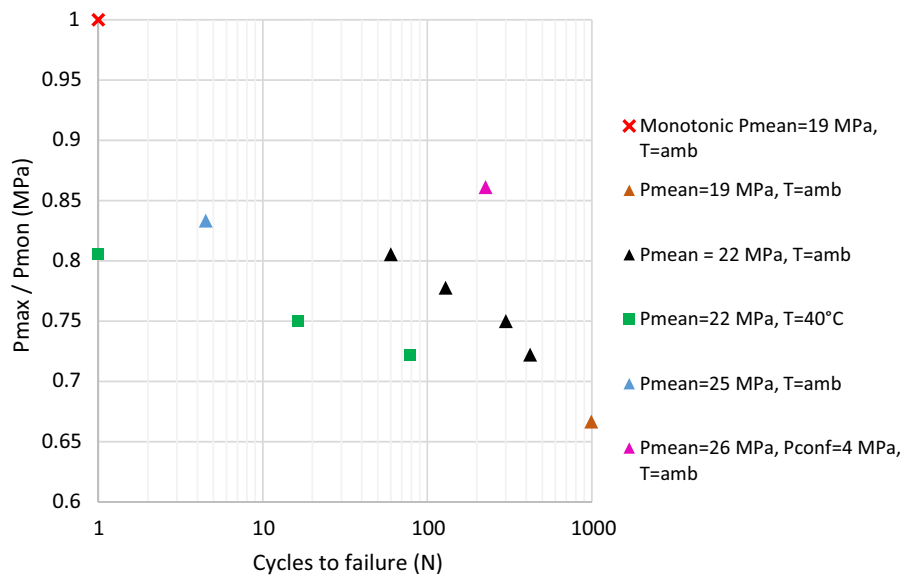
As all experiments failed during the high-pressure portion of the cycle, we can cast this breakdown pressure (P_{max}) in terms of a fraction of the monotonic breakdown pressure (P_{mon}) measured for the room temperature samples. The data is plotted relative to the number of cycles to failure in Fig. 7. Our results show that the higher the maximum pressure of our cycles, the lower the number of cycles to failure. Increasing the mean pressure from 19 MPa (orange triangle) to 22 MPa (black triangles) and 25 MPa (blue triangle) at ambient temperature results in an decreasing number of cycles to failure. This is explored further in Sect. 3.3.3.

The results also indicate weakening of the material as a result of temperature increase, suggested by the shift to failure at lower numbers of cycles for the same pressure conditions (Fig. 7; compare black triangles at ambient temperature to green squares at 40 °C). That reduction is in the order of one order

Table 2 Cycles to failure for each experiment

ID	Maximum pressure	Minimum pressure	Mean pressure	Pressure amplitude	Confining stress	Temperature	Rig	Type	Cycles to Failure
NA	MPa	MPa	MPa	MPa	MPa	°C	NA	NA	Cycle
0	38	0.1	19.05	37.9	0.1	Ambient	Unconfined	Monotonic	N/A
1	29	15	22	14	0.1	Ambient	Unconfined	Cyclic	60
2	28	16	22	12	0.1	Ambient	Unconfined	Cyclic	129
3	27	17	22	10	0.1	Ambient	Unconfined	Cyclic	300
4	26	18	22	8	0.1	Ambient	Unconfined	Cyclic	421
5	26	18	22	8	0.1	Ambient	Unconfined	Cyclic	212
6	24	14	19	10	0.1	Ambient	Unconfined	Cyclic	992
7	30	20	25	10	0.1	Ambient	Unconfined	Cyclic	4.5
8	26	18	22	8	0.1	40 °C	Unconfined	Cyclic	79
9	27	17	22	10	0.1	40 °C	Unconfined	Cyclic	16.5
10	29	15	22	14	0.1	40 °C	Unconfined	Cyclic	< 1
11	31	21	26	10	4	Ambient	GREAT Cell	Cyclic	226

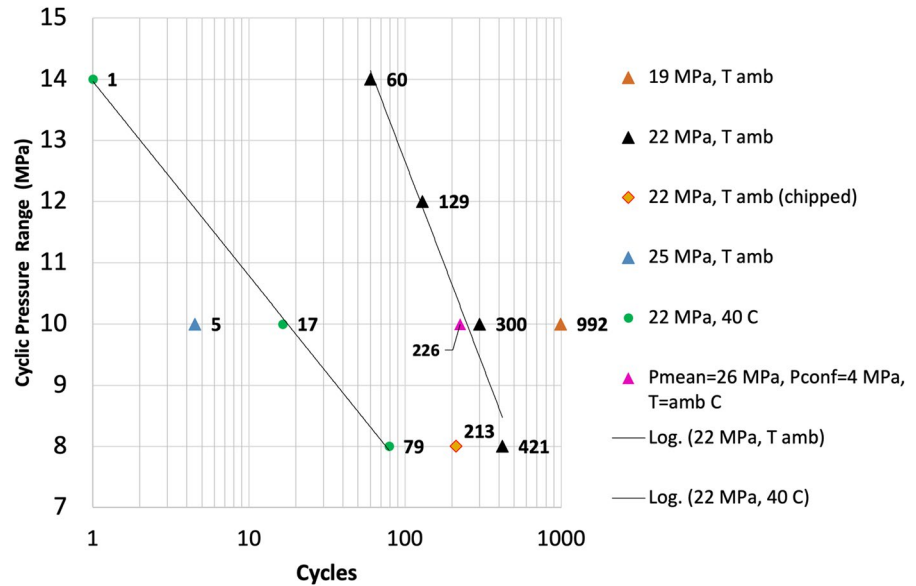
Fig. 7 S–N curves from our study as a fraction of the monotonic breakdown pressure measured under unconfined, room temperature conditions, against cycles to failure. Our results include two experimental temperatures (ambient and 40 °C), confined and unconfined results, all at a frequency of 0.14 Hz



of magnitude of cycles (for samples who have experienced at least 10 cycles). This result is supported by the manufacturer data (Fig. 2), which shows a strength reduction with increasing temperature, noting that the temperature contrast here is chosen to shift the mechanical properties of the analogue material. Here we plot these results with maximum pressure as a fraction of the monotonic breakdown pressure at ambient temperature, to highlight the impact of shifting the material properties.

Finally, the test performed with the addition of confining pressure fractured after a number of cycles consistent with the trend obtained from unconfined tests 1–4 (black triangles), which all had the same mean pressures with varying amplitudes (see Table 2). Indeed, by experimental design, the samples from the confined experiment 11 and the unconfined experiment 3 were exposed to the same differential stress state (effective stress) at the borehole wall. Hence, the differential stress state at the borehole is

Fig. 8 Cyclic pressure amplitude versus cycles to failure, for various mean borehole fluid pressures (indicated in the key). The number by each point is the number of cycles to failure. The results show the inverse relationship between increasing mean stress and decreasing cycles to failure. Note that for the test with confining pressure (pink triangle) the fluid pressure is higher by 4 MPa, but the effective stress at the wellbore wall is equivalent to the unconfined test series with a wellbore fluid pressure of 22 MPa



a key parameter to extrapolate experimental results from unconfined to confined situations. Note that the confined experiment is offset from the unconfined experiments in Fig. 7, but that is due to the normalisation of its maximum pressure by the monotonic breakdown pressure under unconfined conditions, as we did not perform a monotonic test in confinement. Given the comparability of the stress states demonstrated, we would expect the monotonic breakdown pressure under confinement to shift higher accordingly, and the confined condition to then fall into line with the S–N curve of the unconfined case (Fig. 8).

3.3.3 Mean pressure

The effects of mean pressure were investigated by retaining the same pressure amplitude and by varying both minimum and maximum fluid pressure by the same increment.

Three different mean pressures were investigated: 19, 22 and 25 MPa, corresponding to 50%, 58% and 66% of the monotonic breakdown pressure. The majority of our tests were conducted at 22 MPa mean pressure. The results indicate that increasing mean stresses causes a reduction in cycles to failure (though we note that maximum and minimum pressures also shifted due to retaining constant amplitude). In detail, it took 5 cycles to initiate fracture at a mean pressure of 25 MPa compared to 300 cycles at a mean pressure

of 22 MPa, and 992 cycles to fail at a mean pressure of 19 MPa. Interestingly, the experiment under confined conditions with a mean pressure of 26 MPa plots adjacent to the unconfined test at 22 MPa. This would be expected if a linear superposition of the stress states was undertaken as the effective stress would also be 22 MPa in the confined test.

Attention should also be drawn to the minimum stress component of the mean stress. Indeed, experiments 1 and 7 have equivalent maximum pressures of 29 and 30 MPa respectively, but the difference in minimum pressures of 15 and 20 MPa respectively is much greater. The number of cycles to failures in experiment 1 is 60 and that of experiment 7 is 4.5. This highlights that by including variable minimum pressures for equivalent maximum pressure (i.e. increasing the mean pressure when P_{\max} is fixed) lower numbers of cycles to failure can be achieved.

The effects of temperature on the number of cycles to failure is also significant. Tests at 40 °C were conducted with the same primary mean pressure of 22 MPa as was at ambient temperature (~21 °C). Three cyclic pressure amplitudes were tested, and also showed a reduction in cycles to failure at higher amplitude (Fig. 7). Relative to the ambient temperature tests, failure occurred earlier at 40 °C due to the reduced strength of the PMMA at this temperature (Fig. 7).

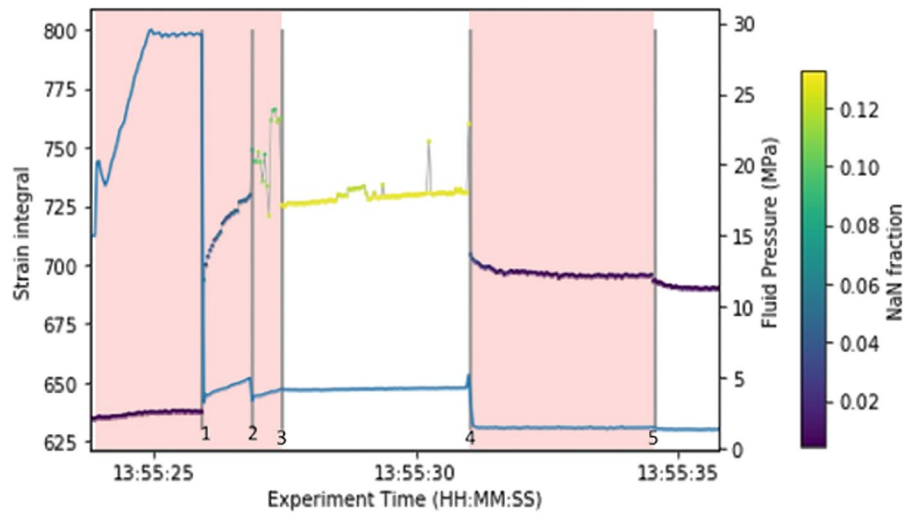


Fig. 9 Correlation between fluid pressure (blue line) and strain on the outside of the sample (variable coloured line). The NaN fraction indicates the fraction of values recorded as NaN by the ODISI-B system. The NaN values come from the measurement accuracy being lower than the quality factor of the ODISI-B module. Grey lines indicate points of interest explained in the main text. Step 1 indicates the first fracture. Step 2 the propagation of the fracture after the new pressure

build up. Step 3 marks the start of the low pressure cycle, where the sample becomes disconnected from the pump and the high-pressure line is able to repressurise to its set point. Step 4, marks the re-exposure of the fractured sample to the repressurised line and the fracture reaching the edge of the sample. Step 5 marks the change to the low-pressure part of the cycle. Shaded areas indicate the high-pressure portions of the cycles

3.4 Pressure–strain: monitoring fracture growth

Here we present the pressure and strain results relating to the best optical dataset showing the growth of the fracture. As it was not possible to predict the direction of the fracture due to the fact the sample was radially unconfined, most of the tests yielded footage unsuitable for the optical analysis, except for Experiment 1, which forms the basis for the following discussions.

The fluid pressure data demonstrate a sharp pressure drop from 29 MPa to 3.5 MPa immediately after the initial fracture stage develops (Fig. 9, step 1). The fluid pressure steadily increases again at a slower rate once the initial fracture has developed. This is due to the high-pressure line still delivering pressurised fluid. It then reaches another threshold at 5 MPa, characterised by a further fracture growth event and fluid pressure drop (Fig. 9, step 2). At this stage the fluid pressure starts to increase again but at an even slower rate, before stabilising at 4 MPa as a result of the solenoid valve switching to the low pressure line (Fig. 9, step 3). It is important to note that the fluid pressure does not increase back to the minimum fluid

pressure set in the experiment. This is due to the low pressure line being disconnected from the pump and only containing a backpressure regulator set to not exceed the minimum pressure for the test. As soon as the solenoid valve switches back to the high pressure line, the pressure increases to 5.6 MPa as fast as in the previous cycles and finally fractures the sample all the way to the sample exterior (Fig. 9, step 4). The fast increase in pressure can be explained by the re-pressurisation of the high pressure line whilst the solenoid valve was switched to the low-pressure part of the cycle. Notably, in both cases the fracture growth pressure is 5–6 MPa, significantly lower than the 29 MPa which caused the initial fracture. The pressure then drops down to about 1 MPa regardless of whether the high or low-pressure lines are connected (Fig. 9, step 5).

The strain data, obtained by the strain gauge surrounding the sample, can be closely correlated to the pressure signal from the fluid line. Strain data are presented as a strain integral in Fig. 9. This was calculated as the sum of the strain data multiplied by the length between each sample point (2.6 mm) on the fibre, to give an indication of the total strain

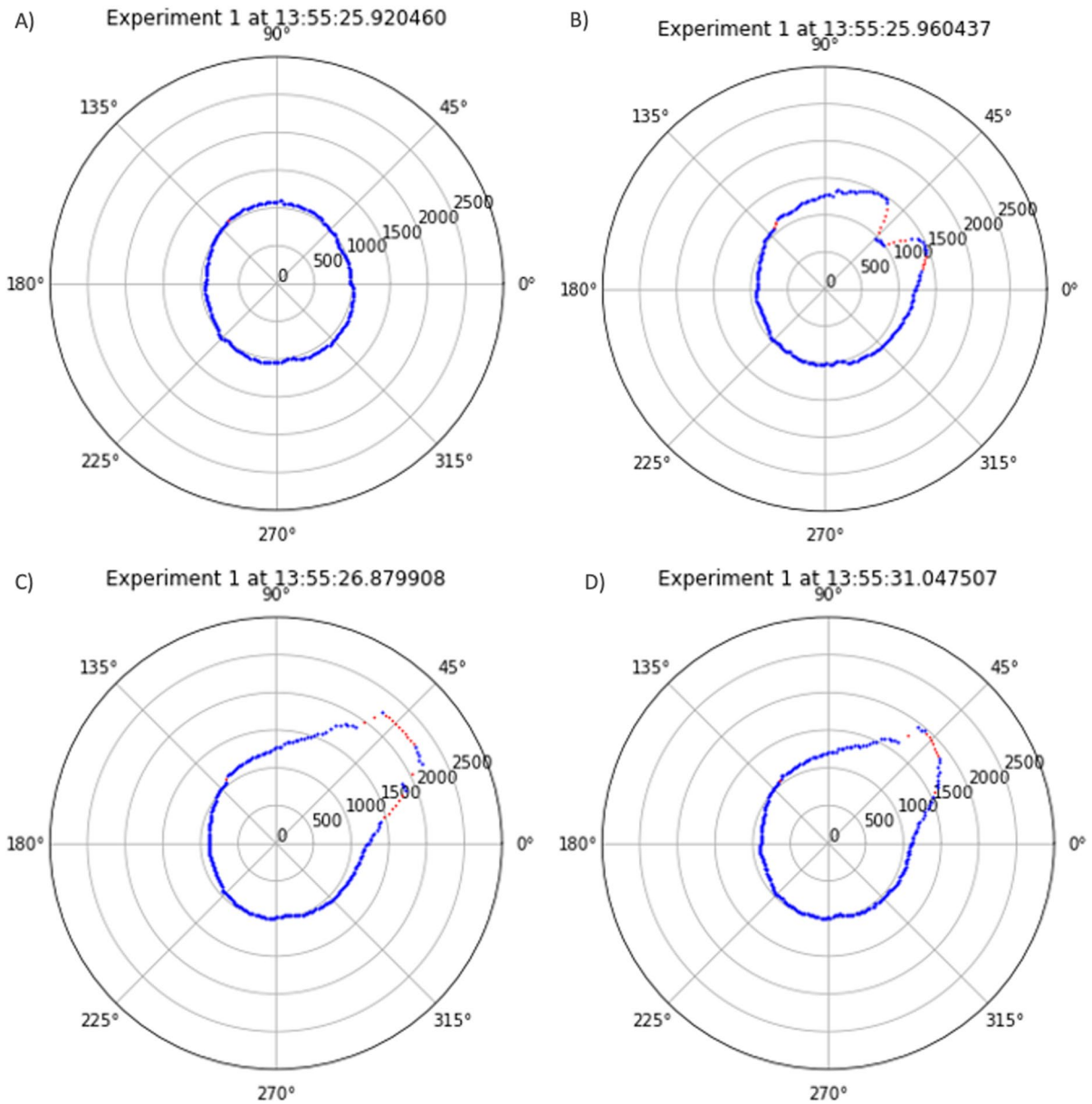


Fig. 10 Fracture stages from Fig. 9. **A** prior to failure, **B** the initial fracture stage, **C** the second fracture stage, during the high-pressure portion of the cycle, the **D** final fracture stage reaching the outside of the sample

around the circumference of the sample through time, for direct comparison to the fluid pressure data. In Fig. 10 the strain data are presented as strain maps that can be considered as exaggerated plan view images of the sample circumference. These show the localisation of the deformation around the location of the propagating fracture. In Fig. 9 the sample reacts to the initial increase in pressure from the low to high

part of the cycle with a slight increase in strain. As soon as the fracture starts to develop (Fig. 9, step 1) a net increase in strain at the outside of the sample can be observed from 500 to 1000 $\mu\epsilon$ (from Fig. 10A, B). Figure 10 B shows the initial growth of the fracture. Then, as the pressure increases, the strain at the outside of the sample also increases. This increase is not large enough to lead to a visually detectable growth

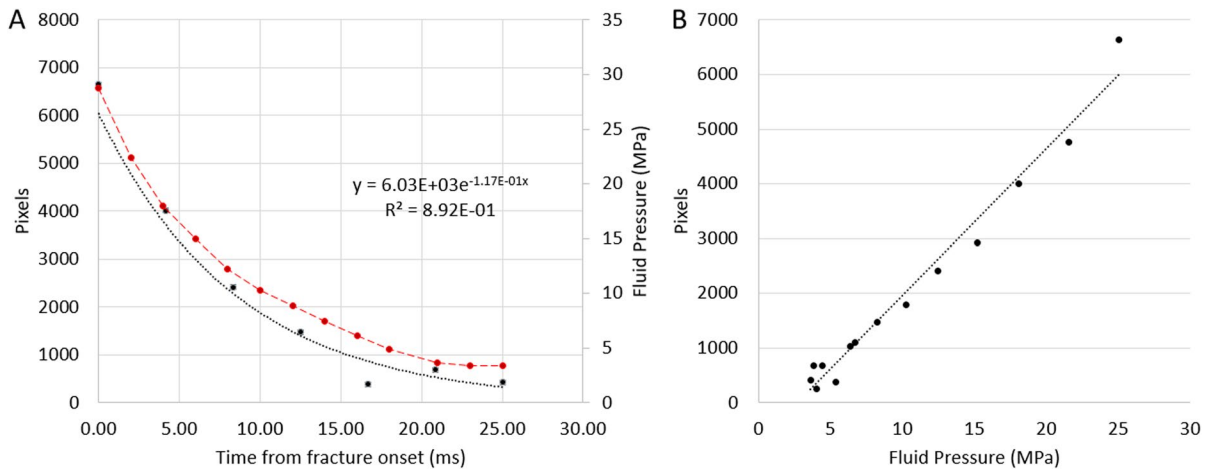


Fig. 11 **A** The reduction in pressure (red), and the reduction in area growth represented by the change in pixels from one frame to the next (black). **B** Correlation between pressure in

the borehole and the growth of the fracture in pixels. This indicates how well the pressure drop can be related to the visual growth of the fracture

of the fracture. As the second fracture stage develops (Fig. 9, step 2), and nears the edge, the strain signal becomes noisy as it starts to drop below the quality factor of the instrumentation in the orientation where the fracture is growing. The NaN values come from the measurement accuracy being lower than the quality factor of the ODISI-B module (i.e. this occurs when a measurement is multiple orders of magnitude greater than the average). These NaN values have been linearly interpolated and are indicated in red in Fig. 10. This increase in NaN values is indicated in the figure by warmer colours. During this secondary fracture growth stage, the strain gauge records greater strain, in excess of $1750 \mu\epsilon$ (Fig. 10C). As the cycle reverts back to the low-pressure line (Fig. 9, step 3), which is not supported by the pump, the strain seems to be increasing at a lower rate, comparable to pre-fracture levels. The data at this stage is of lower quality with 12% of the strain data missing around the fracture area. As the line switches back to the high-pressure and the fracture finally reaches the edge of the sample, the accumulated strain is released (Fig. 9, step 4) which results in the gauge signal recovering its pre-fracture accuracy. This provides confidence that the fracture process does not damage the gauge. The final grey line (Fig. 9, step 5) indicates the change back to the low pressure line, showing a release in strain, to a level slightly below that of the strain after the fracture reached the outside of the sample during the high pressure part of the cycle.

3.5 Pressure–optical: fracture growth

Figure 11 shows that the fracture growth rate, quantified from the pixel count from the image segmentation process, decreases exponentially as the fracture grows during the first stage of fracture propagation (step 1 in Fig. 9). This is also the case for the pressure data. As the fluid pressure drops, the pixel count also drops (Fig. 11B) indicating that the rate of increase of fracture area diminishes as the pressure drops. It should be noted that the strain data cannot be correlated in the same way as the pressure data, because the resolution of the strain data is 40 ms and therefore longer than the analysis time frame of the fluid pressure drop (Fig. 11A). The initial fracture propagation stage progresses through most of the sample and results in a very rapid decrease in the fluid pressure inside the wellbore. The pressure decreases from 29 MPa down to 3.5 MPa during this initial fracture event.

4 Discussion

In this section we will discuss our findings in the context of applying the findings to geo-energy applications. The reported tensile strength of the PMMA is between 77 and 81 MPa at ambient temperature. The breakdown pressure in the monotonic hydraulic fracturing tests is ~ 38 MPa, yielding a differential stress

in the borehole of ~ 73 MPa according to our modelling. This discrepancy can be attributed in part to the strong dependency of tensile strength on the strain rate (Wu et al. 2004). Indeed, Wu et al. (2004) report a tensile strength of PMMA of about 70 MPa at a strain rate of $\sim 1^{-2} \text{ s}^{-1}$ and 41 MPa at $\sim 1^{-5} \text{ s}^{-1}$.

In the axial region of the borehole wall, the modelled values in Fig. 5 are around 3.5% lower than Lamé's analytical answer. The stress distribution in the Lamé solutions for thick-walled cylinders is a function of the cylinder's shape and the pressure boundaries, and is independent of the material properties. Several simulations were made with a lower Poisson's Ratio which had no effect on the response at the bottom of the borehole but reduced the maximum differential stress in the vertical portion of the borehole wall. Hence, the fatigue response of the specimen results from the stress state at the borehole wall. This is consistent with the observations presented in the S–N curves (Fig. 7). We note that in natural geomaterials it is common to have some degree of pre-existing permeability, in that case Gan et al. (2015) invoke other parameters like the interfacial tension of the fluid, which controls the percolation of the fluid into the matrix and affects the breakdown pressure.

Our results show that mean, maximum and minimum pressures, and amplitude of the pressure pulses in the wellbore all impact the fatigue life of the PMMA samples tested. The standardised approaches (usually using dog-bone or notched specimens) used in the literature describe cyclic regimes where the minimum stress is set to 0 MPa (or very close to avoid buckling in case of overshoot). Since this minimum stress parameter is rarely studied in conventional dog-bone testing the effect of the minimum wellbore pressure has, to date, been difficult to quantify. This is particularly relevant to subsurface geomechanics applications where hydraulic cyclic pressure pulses might be applied, in which the existing formation pressure will define the minimum pressure that can be safely achieved.

Our geometry also displays results consistent with existing studies conducted on dog bone and notched samples (Huang et al. 2014; Okeke et al. 2018). In particular, we observe a reduction in the number of cycles to failure with an increase in maximum stress (Fig. 7). We observe that the slope obtained from our experiments is steeper than what has been reported for geomaterials (Cerfontaine and Collin 2018). This

can be explained by the fact we are using PMMA rather than a geomaterial; in PMMA we demonstrated that the Young's Modulus exhibits a time dependence, through the strain rate (Fig. 4), and others have shown the rate dependence of the strength (Wu et al. 2004), as such, our longer duration experiments likely needed to exceed a lower strength, as well as demonstrating the cyclic fatigue. In this study we demonstrate that the effect of the minimum stress during the low pressure part of the cycles also has an impact on the fatigue life of the sample in addition to the maximum stress induced during the high pressure parts of the cycles. Indeed, experiments 1 and 7 have maximum pressures of 29 and 30 MPa respectively, but a much greater difference in minimum pressures of 15 and 20 MPa respectively. The number of cycles to failure in experiment 7 is 4.5 and that of experiment 1 is 60. We attribute this difference to the higher minimum pressure in experiment 7. This has not been demonstrated before in PMMA samples under the studied geometry. This finding has implications for operational practices in geomechanics practices as, if the results up-scale, the operator would reduce both breakdown pressure and number of cycles to failure by increasing P_{\min} , and hence P_{mean} , rather than the amplitude, for a constant P_{\max} . This is also important where P_{\max} might be fixed by regulations, or by the pump's capital cost.

Our results also demonstrate that multi-stage fracture growth can result from cyclic pressurisation. The fluid pressure data from Fig. 9 for experiment 1 showed a gradual increase following the initial fracture stage. This can be attributed to the 'high-pressure' part of the cycle still being active. The rate of pressure increase is lower than at the onset of a cycle prior to a fracture being present. This can be explained by (1) the pump capabilities and (2) the additional volume of the fracture the fluid now has to fill. It takes approximately 1 s for the fluid pressure to reach 5 MPa, at which point the second stage of the fracture propagates again, which can be correlated to the optical data (Fig. 11). Again the re-pressurisation rate decreases slightly, as the pump has to fill a larger volume. It can also be observed that the fracture initiation pressure (29 MPa) is therefore much higher than the fracture growth pressure (5 MPa) this is in accordance with the literature on hydraulic fracturing (Cheng and Zhang 2020). During this secondary fracture growth stage, the strain gauge records greater

strain, in excess of 1750 $\mu\epsilon$. This could be due to the initial fracture stage reaching closer to the edge and hence the strain accommodation during the second stage of the fracture growth happens in a much smaller portion of the material that is closer to the strain gauge. This secondary fracture stage does not extend the initial fracture area significantly. In effect, the strain is more widely distributed during the first fracture propagation because the sample is an intact elastic medium, but once the fracture is present the strain is more localised around the fracture tip, and importantly, the stress that is able to build is lower due to the lower strength that can be sustained in an already fractured medium.

These experiments demonstrate that cyclic pressurisation may be an effective way to implement multi-staged fracturing. This is in contrast to our monotonic tests, which mimic the usual method of creating hydraulic fractures, where a single pervasive fracture extended from the central borehole to the sample margin. Such developments may aid in reducing the largest induced seismic events (caused by large fractures) by facilitating more small fracturing events, as has been proposed by Zang et al. (2021). The ability to control the fracture development in stages using CHPP is beneficial to geoenery applications where carefully controlling the permeability of the near-borehole area is critical to fluid injection and recovery operations. This approach could be used to sequentially increase permeability up to the desired level. It must be noted that further research and development of the pumping equipment would be required to deliver these pressure pulses accurately at depth.

During experiment 10, the heated sample failed during the initial pressure ramp up of the first cycle. This implies that the failure criterion was reached, and the fracture developed in a similar fashion to a monotonic pressure test 12. This is consistent with the strong temperature dependency of the ultimate tensile strength of PMMA (Fig. 2), which reduces as temperature increases (Abdel-Wahab et al. 2017; Gao 2018). This indicates a consistent effect of temperature measured in standardised tensile tests and in our geometry applicable to hydraulic fracturing. It should be noted that although the observation is consistent with the theory, the borehole from the sample test 12 had been partially miss-aligned, leading to more asperities inside the borehole. This

damage could have contributed to stress concentration points. Hence, we do not consider this data point to be quantitatively representative. Nonetheless, tests 8 and 9 provide us with consistent results, clearly indicating that the weakening effect of PMMA by temperature observed in tensile tests translates well to our test geometry. Overall, our results are comparable with existing literature showing that the heating of the PMMA contributes to it failing earlier as temperature increases (Liu et al. 2008). This has implications for the planning of geoenery applications, as here we use the increasing temperature to alter the mechanical properties of the analogue rock, demonstrating the viability of the method in different elastic–plastic regimes.

5 Conclusion

This study has demonstrated the square wave pulsed hydraulic capabilities of a uniaxial and triaxial rig to reduce breakdown pressure using PMMA samples of large size. The results obtained agree with previous work on PMMA fatigue and hydraulic fracturing. Using PMMA, which is homogeneous, allowed us to demonstrate that the proposed stress states developing inside the borehole can be reconciled with the Lamé's solution to within 3.5%. This deviation is to be expected due to the partially penetrating nature of the borehole, and some roughness in the borehole from the drilling process.

In addition to showing that the peak pressure in the borehole is the primary control on reducing the number of cycles to failure, we also show that increasing minimum and mean pressure reduce time to failure. The effect of minimum stress is usually not accounted for in the wider PMMA fatigue testing literature as it is commonly set to near 0 MPa. These results indicate that Cyclic Fluid Pressurisation Systems reduce breakdown pressure, which can reduce the peak power needed to induce fractures in geoenery settings.

Moreover, in our optically clear PMMA samples we could reconcile visual observations with the fluid pressure data and circumferential strain data to dynamically characterise multi-stage fracture growth. This is particularly novel in the hydraulic fracturing literature on rocks, as it is normally harder to characterise the growth of the fracture from anything

other than the pressure drop signal, or post-mortem analysis. The observed staged fracture growth during cyclic pressurisation indicates the potential for using Cyclic Fluid Pressurisation Systems to control damage accumulation and permeability enhancement by the creation of numerous small fractures, and reducing the size and occurrence of large fracturing events that produce large seismic events.

Acknowledgements This research was funded by the EPSRC Smart Pulses for Subsurface Engineering (EP/S005560/1). See details at: <https://gow.epsrc.ukri.org/NGBOViewGrant.aspx?GrantRef=EP/S005560/1> For the purpose of open access, the authors have applied a Creative Commons Attribution (CC BY) licence to any Author Accepted Manuscript version arising. We thank Prof. Y. Lavallée for providing access to the Experimental Volcanology Laboratory at University of Liverpool.

Author contributions Conceptualization: ZKS, CIM; Methodology: AF-H, KE, CIM; Formal analysis and investigation: JM-C, JEK; Writing—original draft preparation: JM-C; Writing—review and editing: JM-C, JEK, AF-H, CIM; Funding acquisition: ZKS, CIM; Materials & Engineering: AL.

Declarations The authors have no financial or non-financial interests.

Open Access This article is licensed under a Creative Commons Attribution 4.0 International License, which permits use, sharing, adaptation, distribution and reproduction in any medium or format, as long as you give appropriate credit to the original author(s) and the source, provide a link to the Creative Commons licence, and indicate if changes were made. The images or other third party material in this article are included in the article's Creative Commons licence, unless indicated otherwise in a credit line to the material. If material is not included in the article's Creative Commons licence and your intended use is not permitted by statutory regulation or exceeds the permitted use, you will need to obtain permission directly from the copyright holder. To view a copy of this licence, visit <http://creativecommons.org/licenses/by/4.0/>.

References

Abdel-Wahab AA, Ataya S, Silberschmidt VV (2017) Temperature-dependent mechanical behaviour of PMMA: Experimental analysis and modelling. *Polym Testing* 58:86–95. <https://doi.org/10.1016/j.polymertesting.2016.12.016>

Bradski G (2000) The OpenCV library. *Dr. Dobb's J Softw Tools* 25:120–123

Carnelli D, Villa T, Gastaldi D, Pennati G (2011) Predicting fatigue life of a PMMA based knee spacer using a multiaxial fatigue criterion. *J Appl Biomater Biomech* 9(3):185–192. <https://doi.org/10.5301/JABB.2011.8917>

Cerfontaine B, Collin F (2018) Cyclic and fatigue behaviour of rock materials: review, interpretation and research perspectives. *Rock Mech Rock Eng* 51(2):391–414. <https://doi.org/10.1007/s00603-017-1337-5>

Cheng Y, Zhang Y (2020) Experimental study of fracture propagation: the application in energy mining. *Energies*. <https://doi.org/10.3390/en13061411>

Cobbing, Dochartaigh O (2007) Hydrofracturing water boreholes in hard rock aquifers in Scotland. *Q J Eng Geol Hydrogeol* 40(2):181. <https://doi.org/10.1144/1470-9236/06-018>

Editorial Committee of Fatigue and Fracture Atlas of PMMA (1987) Fatigue and fracture atlas of PMMA. Science Press, Beijing

Fraser-Harris AP, McDermott CI, Couples GD, Edlmann K, Lightbody A, Cartwright-Taylor A, Kendrick JE, Bron-dolo F, Fazio M, Sauter M (2020) Experimental investigation of hydraulic fracturing and stress sensitivity of fracture permeability under changing polyaxial stress conditions. *J Geophys Res Solid Earth* 125(12):1–30. <https://doi.org/10.1029/2020JB020044>

Frash LP (2014) Laboratory-scale study of hydraulic fracturing in heterogeneous media for enhanced geothermal systems and general well stimulation. Colorado School of Mines. <http://search.proquest.com/docview/1639629768?accountid=14723%5Cnhttp://cf5pm8sz2l.search.serialssolutions.com/?&genre=article&sid=ProQ:&atitle=Laboratory-scale+study+of+hydraulic+fracturing+in+heterogeneous+media+for+enhanced+geothermal+systems+and+gener>

Gan Q, Elsworth D, Alpern JS, Marone C, Connolly P (2015) Breakdown pressures due to infiltration and exclusion in finite length boreholes. *J Petrol Sci Eng* 127:329–337. <https://doi.org/10.1016/j.petrol.2015.01.011>

Gao Z (2018) Creep life assessment craze damage evolution of polyethylene methacrylate. *Advances in Polymer Technologies*, pp 3619–3628. <https://doi.org/10.1002/adv.22146>

Geuzaine C, Remacle J-F (2009) Gmsh: a three-dimensional finite element mesh generator with built-in pre- and post-processing facilities. In: *International Journal for Numerical Methods in Engineering*, vol 0

Gomez Rodriguez DM, Dusseault MB, Gracie R. (2016) Cohesion and fracturing in a transparent jointed rock analogue. In: *The 50th U.S. rock mechanics/geomechanics symposium*. Houston, Texas: ARMA. <https://onepetro.org/ARMAUSRMS/proceedings-abstract/ARMA16/All-ARMA16/ARMA-2016-418/125788>

Guo Y, Yang C, Wang L, Xu F (2018) Study on the influence of bedding density on hydraulic fracturing in shale. *Arab J Sci Eng* 43(11):6493–6508

Guruprasad B, Ragupathy A, Badrinarayanan TS, Venkatesan R (2012) Estimation of fracture length as a mechanical property in hydrofracturing technique using an experimental setup. *Int J Eng Technol* 2(12):1921–1925

Hofmann H, Zimmermann G, Zang A, Yoon JS, Stephansson O, Kim KY, Zhuang L, Diaz M, Min K-B (2018) Comparison of cyclic and constant fluid injection in granitic rock at different scales. In: *Proceedings of the 52nd US rock mechanics/geomechanics symposium*. ARMA, Seattle, pp 18–691

Hofmann H, Zimmermann G, Zang A, Min KB (2018b) Cyclic soft stimulation (CSS): a new fluid injection protocol and

- traffic light system to mitigate seismic risks of hydraulic stimulation treatments. *Geotherm Energy*. <https://doi.org/10.1186/s40517-018-0114-3>
- Huang A, Yao W, Chen F (2014) Analysis of fatigue life of PMMA at different frequencies based on a new damage mechanics model. *Math Probl Eng*. <https://doi.org/10.1155/2014/352676>
- Gifford DK, Kreger ST, Sang AK, Froggatt ME, Duncan RG, Wolfe MS, Soller BJ (2007) Swept-wavelength interferometric interrogation of fiber Rayleigh scatter for distributed sensing applications. In: Udd E (ed) *Fiber optic sensors and applications V*, vol 6770, pp 106–114. SPIE. <https://doi.org/10.1117/12.734931>
- Ibanez WD, Kronenberg AK (1993) Experimental deformation of shale: mechanical properties and microstructural indicators of mechanisms. *Int J Rock Mech Min Sci Geomech Abstr* 30(7):723–734
- Khadraoui S, Hachemi M, Allal A, Rabiei M, Arabi A, Khodja M, Lebouachera SEI, Drouiche N (2020) Numerical and experimental investigation of hydraulic fracture using the synthesized PMMA. *Polym Bull*. <https://doi.org/10.1007/s00289-020-03300-6>
- Kolditz O, Bauer S, Bilke L, Böttcher N, Delfs JO, Fischer T, Görke UJ, Kalbacher T, Kosakowski G, McDermott CI, Park CH, Radu F, Rink K, Shao H, Shao HB, Sun F, Sun YY, Singh AK, Taron J, Walther M, Wang W, Watanabe N, Wu Y, Xie M, Xu W, Zehner B (2012) ‘OpenGeoSys: an open-source initiative for numerical simulation of thermo-hydro-mechanical/chemical (THM/C) processes in porous media. *Environ Earth Sci* 67(2):589–599. <https://doi.org/10.1007/s12665-012-1546-x>
- Lee H, Jeon S (2011) An experimental and numerical study of fracture coalescence in pre-cracked specimens under uniaxial compression. *Int J Solids Struct* 48(6):979–999. <https://doi.org/10.1016/j.ijsolstr.2010.12.001>
- Liu W, Gao Z, Yue Z (2008) Steady ratcheting strains accumulation in varying temperature fatigue tests of PMMA. *Mater Sci Eng A* 492(1–2):102–109. <https://doi.org/10.1016/j.msea.2008.03.042>
- Liu Z, Lu Q, Sun Y, Tang X, Shao Z, Weng Z (2019) Investigation of the influence of natural cavities on hydraulic fracturing using phase field method. *Arab J Sci Eng* 44(22):10481–10501
- McDermott CI, Fraser-Harris A, Sauter M, Couples GD, Edlmann K, Kolditz O, Lightbody A, Somerville J, Wang W (2018) New experimental equipment recreating georeservoir conditions in large, fractured, porous samples to investigate coupled thermal, hydraulic and polyaxial stress processes. *Sci Rep* 8(1):1–12. <https://doi.org/10.1038/s41598-018-32753-z>
- Mighani S, Lockner DA, Kilgore B, Sheibani F, Evans B (2018) Interaction between hydraulic fracture and a preexisting fracture under triaxial stress conditions. In: *Society of petroleum engineers—SPE hydraulic fracturing technology conference and exhibition, HFTC 2018*, pp 1–22 (2018). <https://doi.org/10.2118/189901-ms>
- Mohammad R, Zhang S, Al Qadasi A (2018) Investigation of cyclic CO₂ injection process with nanopore confinement and complex fracturing geometry in tight oil reservoirs. *Arab J Sci Eng* 43(11):6567–6577
- Molina O, Vilarasa V, Zeidouni M (2017) Geologic carbon storage for shale gas recovery. *Energy Procedia* 114:5748–5760. <https://doi.org/10.1016/j.egypro.2017.03.1713>
- Okeke CP, Thite AN, Durodola JF, Greenrod MT (2018) A novel test rig for measuring bending fatigue using resonant behaviour. *Procedia Struct Integr* 13:1470–1475. <https://doi.org/10.1016/j.prostr.2018.12.303>
- Okeke CP, Thite AN, Durodola JF, Greenrod MT (2019) Fatigue life prediction of Polymethyl methacrylate (PMMA) polymer under random vibration loading. *Procedia Struct Integr* 17:589–595. <https://doi.org/10.1016/j.prostr.2019.08.079>
- Roshankhah S, Marshall JP, Tengattini A, Ando E, Rubino V, Rosakis AJ, Viggiani G, Andrade JE (2018) Neutron imaging: a new possibility for laboratory observation of hydraulic fractures in shale? *Geotech Lett* 8(4):316–323. <https://doi.org/10.1680/jgele.18.00129>
- Senseny PE, Pfeifle TW (1984) Fracture toughness of sandstones and shales. In: *25th US Symposium on Rock Mechanics*, Evanston, Illinois, June, ARMA. <https://onepetro.org/ARMAUSRMS/proceedings-abstract/ARMA84/All-ARMA84/ARMA-84-0390/131300>
- Swallowe GM, Lee SF (2006) Quasi-static and dynamic compressive behaviour of poly(methyl methacrylate) and polystyrene at temperatures from 293 K to 363 K. *J Mater Sci* 41(19):6280–6289. <https://doi.org/10.1007/s10853-006-0506-9>
- Wanniarachchi WAM, Ranjith PG, Perera MSA, Rathnaweera TD, Zhang DC, Zhang C (2018) Investigation of effects of fracturing fluid on hydraulic fracturing and fracture permeability of reservoir rocks: an experimental study using water and foam fracturing. *Eng Fract Mech* 194(December 2017):117–135. <https://doi.org/10.1016/j.engfractmech.2018.03.009>
- Wu H, Ma G, Xia Y (2004) Experimental study of tensile properties of PMMA at intermediate strain rate. *Mater Lett* 58(29):3681–3685. <https://doi.org/10.1016/j.matlet.2004.07.022>
- Wu R, Germanovich LN, Van Dyke PE, Lowell RP (2007) Thermal technique for controlling hydraulic fractures. *J Geophys Res Solid Earth*. <https://doi.org/10.1029/2005JB003815>
- Xing P (2018) Hydraulic fracture containment in layered reservoirs. M. S. in *Structural Engineering*. http://d-schol.arship.pitt.edu/33432/1/PengjuXing_etdPitt2017.pdf
- Zang A, Zimmermann G, Hofmann H, Stephansson O, Min KB, Kim KY (2019) How to reduce fluid-injection-induced seismicity. *Rock Mech Rock Eng* 52(2):475–493. <https://doi.org/10.1007/s00603-018-1467-4>
- Zang A, Zimmermann G, Hofmann H, Niemann P, Kim KY, Diaz M, Zhuang L, Yoon JS (2021) Relaxation damage control via fatigue-hydraulic fracturing in granitic rock as inferred from laboratory-, mine-, and field-scale experiments. *Sci Rep* 11(1):1–16. <https://doi.org/10.1038/s41598-021-86094-5>
- Zhuang L, Kim KY, Jung SG, Diaz M, Min K-B, Park S, Zang A, Stephansson O, Zimmermann G, Yoon JS (2018) Cyclic hydraulic fracturing of cubic granite samples under triaxial stress state with acoustic emission, injectivity and fracture measurements. In: *Proceedings of the 52nd US*

rock mechanics/geomechanics symposium. ARMA, Seattle, pp 18–297

Zhuang L, Jung SG, Diaz M, Kim KY, Hofmann H, Min KB, Zang A, Stephansson O, Zimmermann G, Yoon JS (2020) Laboratory true triaxial hydraulic fracturing of granite under six fluid injection schemes and grain-scale fracture observations. *Rock Mech Rock Eng.* <https://doi.org/10.1007/s00603-020-02170-8>

Zimmermann G, Zang A, Stephansson O, Klee G, Semiková H (2019) Permeability enhancement and

fracture development of hydraulic in situ experiments in the Äspö Hard Rock Laboratory, Sweden. *Rock Mech Rock Eng* 52(2):495–515. <https://doi.org/10.1007/s00603-018-1499-9>

Publisher's Note Springer Nature remains neutral with regard to jurisdictional claims in published maps and institutional affiliations.